Intermediate Intraseasonal Variability in the Western Tropical Pacific Ocean: Meridional Distribution of Equatorial Rossby Waves Influenced by a Tilted Boundary

ZHIXIANG ZHANG

Key Laboratory of Ocean Circulation and Waves, Institute of Oceanology, Center for Ocean Mega-Science, Chinese Academy of Sciences, Qingdao, and University of Chinese Academy of Sciences, Beijing, China

LARRY J. PRATT

Woods Hole Oceanographic Institution, Woods Hole, Massachusetts

FAN WANG

Key Laboratory of Ocean Circulation and Waves, Institute of Oceanology, Center for Ocean Mega-Science, Chinese Academy of Sciences, Qingdao, and University of Chinese Academy of Sciences, Beijing, and Qingdao National Laboratory for Marine Science and Technology, Qingdao, China

JIANING WANG

Key Laboratory of Ocean Circulation and Waves, Institute of Oceanology, Center for Ocean Mega-Science, Chinese Academy of Sciences, and Qingdao National Laboratory for Marine Science and Technology, Qingdao, China

SHUWEN TAN

Key Laboratory of Ocean Circulation and Waves, Institute of Oceanology, Center for Ocean Mega-Science, Chinese Academy of Sciences, Qingdao, and University of Chinese Academy of Sciences, Beijing, China

ABSTRACT

Intermediate-depth intraseasonal variability (ISV) at a 20–90-day period, as detected in velocity measurements from seven subsurface moorings in the tropical western Pacific, is interpreted in terms of equatorial Rossby waves. The moorings were deployed between 0° and 7.5°N along 142°E from September 2014 to October 2015. The strongest ISV energy at 1200 m occurs at 4.5°N. Peak energy at 4.5°N is also seen in an eddy-resolving global circulation model. An analysis of the model output identifies the source of the ISV as short equatorial Rossby waves with westward phase speed but southeastward and downward group velocity. Additionally, it is shown that a superposition of first three baroclinic modes is required to represent the ISV energy propagation. Further analysis using a 1.5-layer shallow water model suggests that the first meridional mode Rossby wave accounts for the specific meridional distribution of ISV in the western Pacific. The same model suggests that the tilted coastlines of Irian Jaya and Papua New Guinea, which lie to the south of the moorings, shift the location of the northern peak of meridional velocity oscillation from 3°N to near 4.5°N. The tilt of this boundary with respect to a purely zonal alignment therefore needs to be taken into account to explain this meridional shift of the peak. Calculation of the barotropic conversion rate indicates that the intraseasonal kinetic energy below 1000 m can be transferred into the mean flows, suggesting a possible forcing mechanism for intermediate-depth zonal jets.

1. Introduction

The Pacific equatorial ocean plays many roles in regional and global circulation and climate, including the El Niño–Southern Oscillation (ENSO) phenomenon, the Pacific decadal oscillation (PDO), and the Indonesian Throughflow (ITF). The equator acts as a waveguide for

---

eastward and westward propagating disturbances, providing a dynamical connection between the eastern and western coasts. Communication between the tropics and midlatitudes can occur in the ocean via coastally trapped waves and in the atmosphere through poleward propagation of Rossby waves (the atmospheric "bridge"). The tropical ocean is also notable in its abundance of alternating jets, including well-known near-surface examples such as the North/South Equatorial Current and Equatorial Undercurrent (e.g., Johnson et al. 2002), but also alternating zonal jets at greater depths (e.g., Cravatte et al. 2012, 2017).

The structure and variability of tropical Pacific upper ocean circulation have been extensively observed with the aid of satellite and shipboard/lowered acoustic Doppler current profilers (ADCPs), and their dynamical mechanisms have been widely explored (e.g., Wyrtki and Kendall 1967; Wyrtki 1974; Kessler and Taft 1987; Delcroix et al. 1992; Reverdin et al. 1994; Kleeman et al. 1999; Bonjean and Lagerloef 2002; Johnson et al. 2002; Gouriou et al. 2006; Cravatte et al. 2017). However, observations of middepth currents below 1000 m are sparse and there remain large gaps in our understanding of their structure, variability, and dynamics.

The analysis of Argo floats' drifts in the equatorial Pacific (Cravatte et al. 2012, 2017) suggests a series of alternating westward and eastward zonal jets at 1000- and 1500-m depth, with a meridional scale of approximately 1.5°, flowing across the basin over 10°S–10°N. The flow speeds of these intermediate jets decrease from the western to the eastern basins. Based on numerical results and analytical solutions, the ISV has been established as the energy source for the formation of the zonal jets through an inverse energy cascade processes over 3°S–3°N (d'Orgeville et al. 2007; Hua et al. 2008; Ascani et al. 2015) and in the area north of 9°N (Qiu et al. 2013). However, the full system of meridionally alternating zonal jets in the tropical Pacific Ocean still needs to be explained (Ménesguen et al. 2019).

Several scenarios have been proposed for the origin of the intermediate equatorial ISV. First, ISV is produced at depth by the instability of the deep current in the vicinity of the western boundary (Ascani et al. 2015). Second, surface ISV energy such as that due to tropical instability waves can radiate into the deep ocean as a downward- and eastward-propagating beam of Yanai waves (Ascani et al. 2010). Third, wind stress anomalies such as those caused by the Madden–Julian oscillation could give rise to the intermediate ISV through eastward- and downward-propagating oceanic equatorial Kelvin waves (Matthews et al. 2007). Finally, when a low-frequency Kelvin wave propagates through an area with submarine ridge topography, it may give rise to the
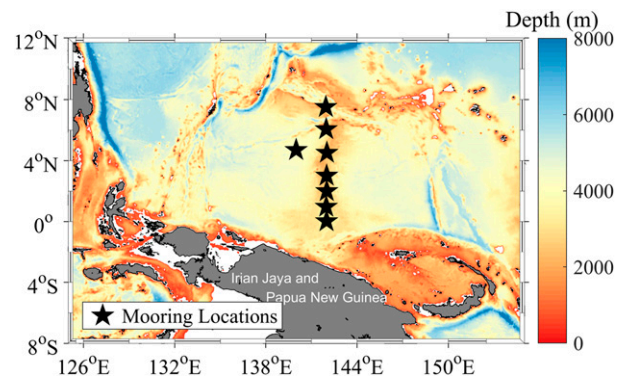

FIG. 1. The locations of subsurface moorings between 0° and 7.5°N along 142°E and at 4.7°N, 140°E, and surrounding topography in the western Pacific Ocean.

middepth ISV of meridional velocity (McPhaden and Gill 1987; Bunge et al. 2008). The generation mechanism of intermediate ISV is still an open question, and thus requires further observations and studies.

Recently, we deployed a subsurface mooring array along 142°E and obtained a 1-yr-long record of intermediate currents. This mooring array is a part of the Scientific Observing Network of the Chinese Academy of Sciences (CASSON) in the western Pacific. We will present the observed meridional structure of ISV captured by this data and explore its underlying dynamics with the help of an eddy-resolving model and a 1.5-layer shallow water model. The paper is organized as follows: section 2 describes the observations and model setups in detail. Section 3 presents observed and modeled features of ISV in the western tropical Pacific. A dynamical interpretation is given in section 4. In section 5, we present a discussion on the relationship between the intermediate ISV and zonal jets by calculating the barotropic conversion rate. The paper concludes with section 6, in which the main findings of the study are summarized.

2. Observation and models

Seven subsurface moorings were deployed on Eauripik rise between 0° and 7.5°N along 142°E to monitor the ocean currents in the far western tropical Pacific Ocean from September 2014 to October 2015 (Fig. 1). Each mooring had one upward-looking and one downward-looking 75-kHz TRDI ADCP, mounted on the main float at approximately 500 m. Each mooring also supported five Nortek Aquadopp or JFE INFINITY-Deep current meters at depths of 1200, 1400, 1600, 1800, and 2000 m and five SBE37 conductivity–temperature–depth (CTD) instruments (Wang et al. 2016a,b). This study concentrates on the instruments at 1200 and 1600 m, since there are some missing data at the other depths

due to instrument failure and loss. Besides the mooring array along 142°E, this study also uses current data over 800–1200-m depths from September 2014 to October 2015 observed by the ADCP at 4.7°N, 140°E. The hourly velocity data are averaged daily to remove tidal signals.

To aid in the interpretation of the observations, we utilize outputs from the eddy-resolving simulation of the Oceanic General Circulation Model for the Earth Simulator (OFES) (Masumoto et al. 2004; Sasaki et al. 2008). The model is based on the third version of the Modular Ocean Model and covers a near-global domain, extending from 75°S to 75°N, with a horizontal resolution of 0.1° × 0.1°. The vertical resolution varies from 5 m near the surface to 330 m near the bottom, with a total of 54 levels. The 3-day snapshot model outputs during the period of 1980–2014 are used in this article.

We also employ a linearized, 1.5-layer and reduced-gravity model, consisting of an active upper layer and an underlying infinitely deep abyssal layer. The motion is assumed to take place on an equatorial β plane and the equations governing the motion in the upper layer are (Yang and Price 2000)

$$\frac{\partial u}{\partial t} - \beta y v = -g'\frac{\partial \eta}{\partial x} + \frac{\tau^x}{\rho_0 h} + A_H\left(\frac{\partial^2 u}{\partial^2 x} + \frac{\partial^2 u}{\partial^2 y}\right), \quad (1)$$

$$\frac{\partial v}{\partial t} + \beta y u = -g'\frac{\partial \eta}{\partial y} + \frac{\tau^y}{\rho_0 h} + A_H\left(\frac{\partial^2 v}{\partial^2 x} + \frac{\partial^2 v}{\partial^2 y}\right), \quad \text{and} \quad (2)$$

$$\frac{\partial \eta}{\partial t} + \frac{\partial h u}{\partial x} + \frac{\partial h v}{\partial y} = 0, \quad (3)$$

where t is time, η is the deviation from the mean layer thickness, h is the mean layer thickness and is chosen as ~1800 m to avoid the presence of layer vanishing, $\beta = \partial f/\partial y$ is the derivative of the Coriolis parameter in the meridional direction, u and v are the horizontal zonal and meridional velocities, $g' = g\Delta\rho/\rho_0 \sim 0.4 \, \mathrm{cm \, s^{-2}}$ (g is gravity, ρ_0 is the water density, and $\Delta\rho$ is the density difference between two layers) is the reduced gravity, τ^x and τ^y are zonal and meridional wind stresses, respectively, and $A_H \sim 2500 \, \mathrm{m^2 \, s^{-1}}$ is the lateral friction coefficient. This model is set in an idealized basin with a flat bottom and rigid lateral boundaries, and is identical to the barotropic shallow water model except that g is replaced by g'.

3. Observed and simulated intermediate intraseasonal variability

a. Observed characteristics along 142°E

The time series of the original velocity vectors at 1200- and 1600-m depths over 0°–7.5°N during September

2014–October 2015 are shown in Figs. 2a and 2d. Observed currents at 1200 and 1600 m at different latitudes are dominated by alternating eastward and westward zonal jets, with a mean zonal velocity generally much larger than the meridional component. At 1200 m, the mean flow is westward at the equator, 1°, 3°, 6°, and 7.5°N, and is eastward at 2° and 4.5°N (Figs. 2c,f). The flow speed is large near the equator, reaching a maximum at 2°N at 1200-m depth and decreases poleward. The meridional structure of the sign and amplitude of mean zonal flows at 1200 m is generally consistent with that of the mean zonal Lagrangian velocities at 1000 m obtained from the tracks of Argo floats (Cravatte et al. 2012, their Fig. 2a), and also that of observed velocities at 1200 m obtained from shipboard ADCP (Cravatte et al. 2017, their Fig. 6a).

To extract the ISV of observed currents, we apply a 20–90-day Lanczos bandpass filter (Duchon 1979) to the original zonal and meridional velocity anomalies, resulting in the time series shown in Figs. 2b and 2e. The ratio between the ISV and the total variance in meridional component V (39%) is much larger than that in the zonal component U (7%), consistent with previous studies in the tropical Indian and Atlantic oceans (e.g., Ponte and Gutzler 1992). In the following, we only focus on the ISV of V. For meridional distributions at 1200 and 1600 m, the spectral energy of the bandpass-filtered V (Figs. 3a,b) both show two peaks, one near the equator and a second near 4.5°N, both with maximum energy at period of about 45 days. The amplitude of the peak at 4.5°N is 3.5 cm s^{-1} at 1200 m but is reduced to 2.1 cm s^{-1} at 1600 m (Fig. 3b).

The vertical distribution of the observed ISV at 4.5°N, 142°E (Fig. 3c) shows two peaks, the upper one at a depth shallower than 200 m and the intermediate one between 900 and 1200 m. The exact position of the intermediate peak cannot be determined due to the low vertical resolution (~200 m) of our instruments below 1000 m. The upper peak may result from eddy activity (Wang et al. 2016a) and the explanation for the intermediate peak will be explored in the following sections.

b. OFES simulated characteristics

The striking feature of the mooring array results along 142°E is that the largest amplitude of ISV is located at 4.5°N. To explore the underlying mechanisms, we examine the eddy-resolving OFES model results. We begin by evaluating the OFES ability to simulate the ISV in the western tropical Pacific Ocean, comparing the spectral energy of the observed and modeled 20–90-day bandpass-filtered V at 1200 m (Figs. 3a and
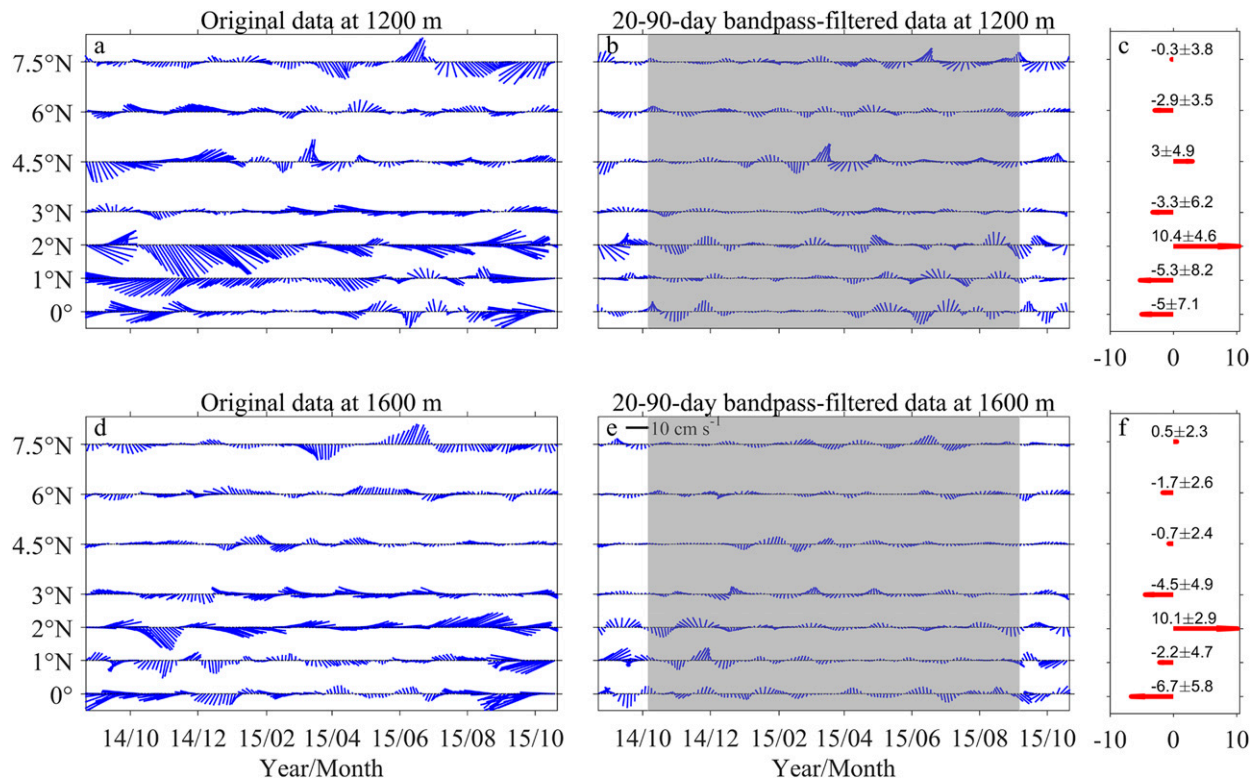
FIG. 2. (a),(d) Original and (b),(e) 20–90-day bandpass-filtered anomalous daily current velocity vectors (cm s^{-1}) measured by moored current meters along 142°E during September 2014–October 2015 at depths of (top) 1200 and (bottom) 1600 m. (c),(f) The corresponding mean zonal flow speed and direction, given by arrows, and where the number denotes the mean $\pm$ standard deviation of zonal velocity (cm s^{-1}). The gray shaded areas denote the time series without edge effects.

4a). The spectral energy of OFES ISV shows a primary peak at 4.5°N and a secondary peak near the equator. This meridional pattern greatly resembles those of the mooring results, although the intensity of OFES ISV is stronger and the peak period is longer. For the vertical distribution at 4.5°N, the spectral energy of OFES ISV shows two peaks at the depths shallower than 200 m and over 600–800 m, respectively (Fig. 4b). The depth of intermediate peak (around 800 m) is shallower than that in our observations. The qualitative agreement between OFES and our observations leads to analyses the OFES simulation further to identify the mechanisms responsible for the observed intermediate ISV.

Before proceeding further, we note that the full 35-yr time series of OFES data was examined in order to check whether there is interannual change in the meridional structure of ISV along 142°E. The spectral energy of the 20–90-day bandpass-filtered currents over a 3-yr moving segment shows peaks that remain at approximately 4.5°N (figures not shown). This suggests that the ISV meridional distribution is not strongly affected by interannual variability.

4. Dynamical interpretation of intermediate intraseasonal variability

a. Linkage between intraseasonal variability and Rossby waves

A connection between wave propagation and ISV at 4.5°N is evident in time–longitude plots of the original and 20–90-day bandpass-filtered OFES V at 1200 m during 2012–14 (Fig. 5). The phase of signal propagates westward and takes approximately 3 months from the mooring site (142°E) to 132°E, as indicated by the black solid line in Fig. 5b. There are periods when the amplitudes are strong near 142°E, for example, September–December 2012 and August–December 2013. The phase speed is approximately 14 cm s^{-1}, and the zonal wavelength is about 500 km. We conduct cross-spectral analyses of the OFES meridional velocities between each depth and 1200 m to obtain the phase lag profile (Fig. 4c). The meridional disturbance velocity at 1200 m shows a gradual increase in phase by about 90° from 1800 to 300 m, with a sharp increase of about 180° from 300 to 250 m.

A wavenumber–frequency analysis of OFES meridional velocities along 4.5°N between 128° and 160°E and
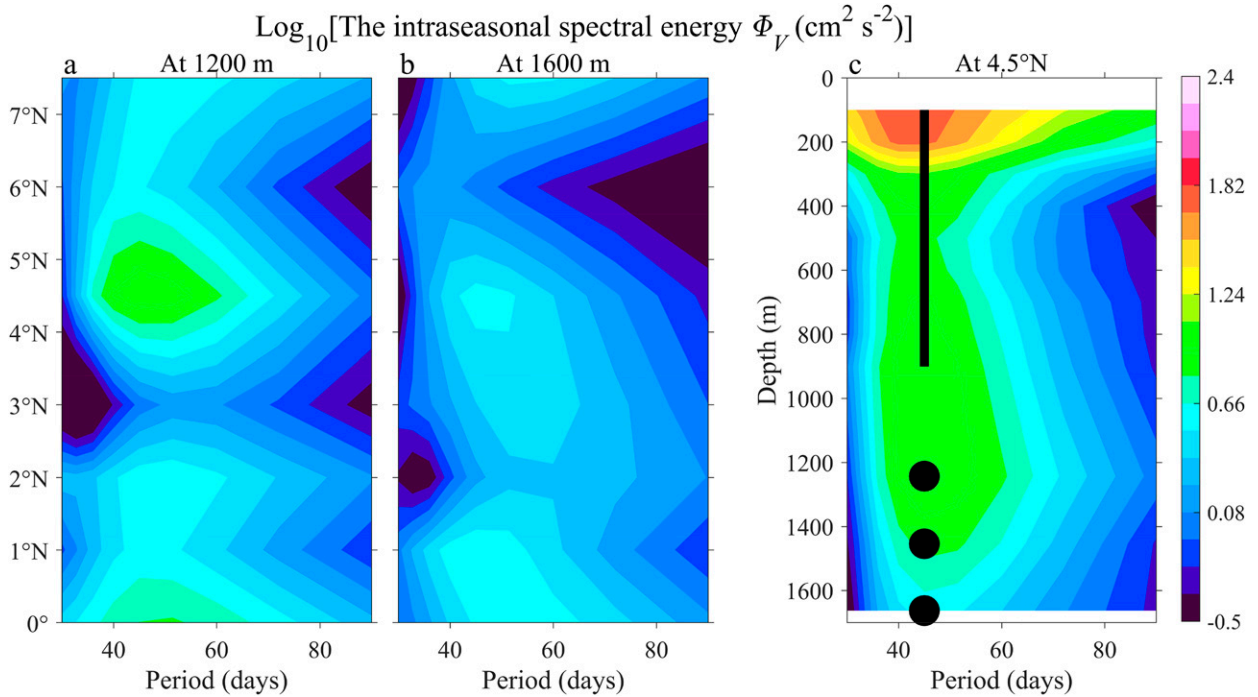
FIG. 3. Meridional distributions of logarithmic intraseasonal spectral energy based on meridional velocity V at (a) 1200 and (b) 1600 m. (c) Vertical structure of logarithmic intraseasonal spectral energy at 4.5°N. In (c), the black line and circles indicate the mean locations of ADCP velocity profiles and current meters, respectively. Intraseasonal spectral energy values are obtained using a 20–90-day bandpass-filtered daily V from mooring observations.

over 1980–2014, using a two-dimensional fast Fourier transform (Zang et al. 2002; Farrar and Weller 2006; Farrar 2008, 2011), is performed to determine the type of waves that could explain the ISV. The area with the most significant spectral energy corresponds to waves with a period of 40–60 days and a wavelength of 400–700 km (Fig. 6). Also appearing in Fig. 6 are the dispersion curves for the first three baroclinic and first two meridional modes of Rossby waves, which all go through the most significant spectral energy area. The corresponding dispersion relation is (Matsuno 1966; Lighthill 1969; Pedlosky 1987)

$$\omega = -\frac{\beta k c_n}{k^2 c_n + (2j+1)\beta}, \tag{4}$$

where ω is the wave frequency, k is horizontal wavenumber, j and n indicate meridional and baroclinic mode numbers, respectively, and c_n is the characteristic speed of the nth baroclinic mode. The values of c_n (Table 1) are obtained by solving the standard eigenvalue problem for hydrostatic motion with constant depth H (Shankar et al. 1996)

$$\left(\frac{1}{N^2}\varphi_{nz}\right)_z = -\frac{1}{c_n^2}\varphi_n(z), \quad n = 0, 1, 2, \ldots, \tag{5}$$

and subject to the boundary conditions $\varphi_{nz}(0) = \varphi_{nz}(-H) = 0$. Here $\varphi_n(z)$ denotes vertical normal eigenfunctions, $N^2 = -(g/\rho)(\partial\rho/\partial z)$ is the squared Brunt–Väisälä frequency, and ρ is obtained from the climatological density profile at 4.5°N, 142°E from the *World Ocean Atlas 2013* (*WOA13*). Subscript z represents the vertical derivative. The eigenfunction corresponding to $n = 0$ represents the barotropic mode and $n \geq 1$ indicates the nth baroclinic mode. It should be noted that equatorial Rossby waves with baroclinic modes larger than three ($n > 3$) do not exist in the intraseasonal frequency band (Table 1); hence we only consider the first three baroclinic modes in the following.

Significantly, the area of strongest energy area is located to the left of the maximum of these curves, which indicates eastward group velocity (i.e., $\partial\omega/\partial k > 0$). This implies that all of first three baroclinic mode short Rossby waves are the candidates for the propagation for intermediate ISV. However, the dispersion relation [Eq. (4)] only applies to an infinite domain with no horizontal boundary, whereas the coastlines of Irian Jaya and Papua New Guinea lie south of the mooring array (Fig. 1). Philander (1977) addressed the problem of equatorial waves in the presence of a purely zonal (nontilted) boundary and derived the modified dispersion relation

Log$_{10}$[The intraseasonal spectral energy Φ_V (cm^2 s^{-2})]
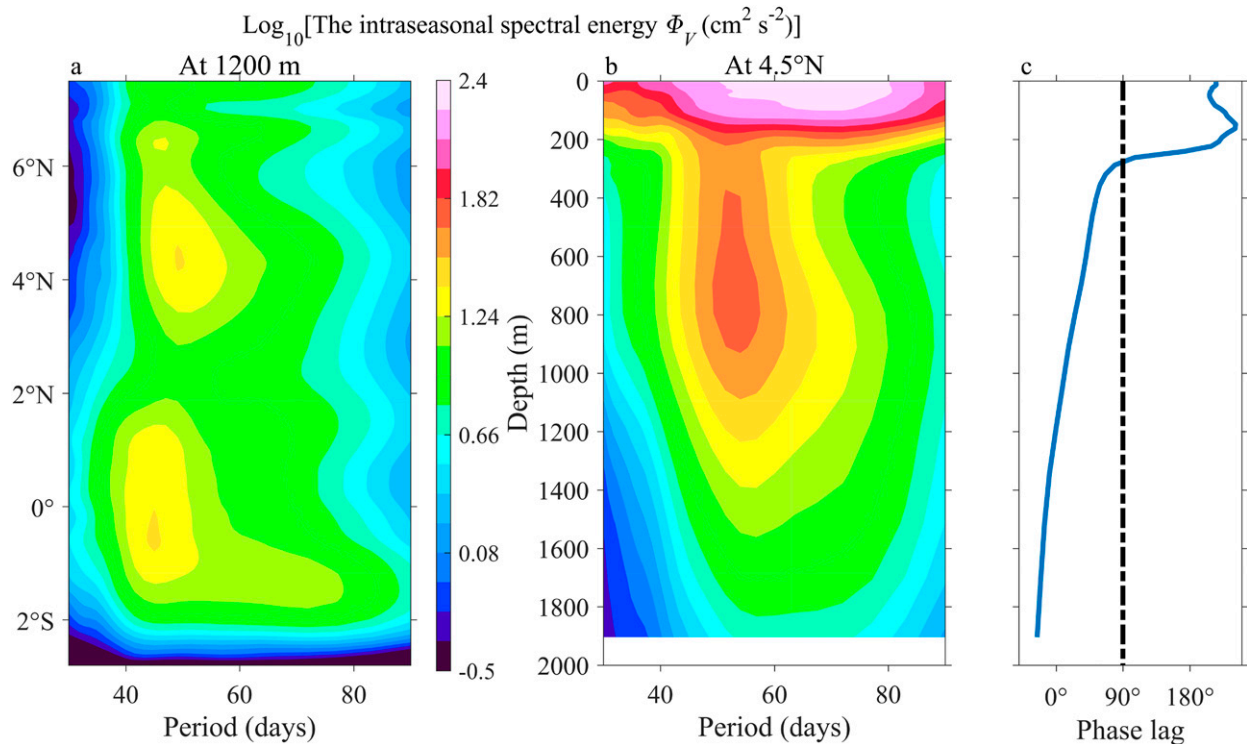

FIG. 4. (a),(b) As in Figs. 3a and 3c, but based on the OFES data during 1980–2014. (c) Vertical profile of the phase lag for the 50-day period, obtained from cross-spectral analyses of the OFES V between each depth and 1200 m. The phase lag of 90° is denoted by the black dashed line.

$$\frac{\omega^2}{c_n^2} - k^2 - \frac{\beta k}{\omega} - \frac{\beta}{c_n}(2\nu_j + 1) = 0, \quad j = 0, 1, 2 \ldots, \quad (6)$$

where ν_j is the jth root of the indicial equation. It should be noted that Eq. (6) also includes gravity wave behavior while Eq. (4) only contains Rossby wave. His results suggest that the zonal coastline can potentially alter the meridional structures of equatorial Rossby waves. Our situation is even more complex since the coastlines of Irian Jaya and Papua New Guinea tilt roughly from west-northwest to east-southeast, which means that the usual separation of zonal and meridional structure of the Rossby wave is no longer valid, and that a simple analytical theory is apparently no longer possible. We therefore attempt to address this issue using a numerical model, as described below.

b. The meridional structure of ISV energy influenced by a tilted southern boundary

Moore and McCreary (1990) confronted a somewhat similar situation in their investigation of a tilted western boundary and its influence on forced equatorial waves in the Indian Ocean. They approached the problem by forcing a model with different fluctuating wind stress distributions in order to study different types of

equatorial waves in isolation. We take a similar approach, using the 1.5-layer model with different wind forcings to produce specific Rossby waves. We then note the effect of the tilted boundary on the meridional structure of each wave. The computational domain spans 20°S–20°N and 128°–188°E (Fig. 7a). A tilted southern boundary from 0°, 128°E to 5°S, 148°E is imposed to represent the northern coasts of Irian Jaya and Papua New Guinea. In the model setup, two kinds of wind stress fields (Figs. 7b,c) are introduced in the open equatorial region (5°S–5°N, 175°E–175°W) to trigger equatorial Rossby waves that would have odd and even meridional modes in the absence of a tilted boundary (referred as odd and even mode cases in the following). The periods of both wind stress distributions are set to 50 days to represent an ISV oscillation. The detailed settings of wind stress fields are given in Table 2.

Since the wind stress forcing is imposed east of the region of interest, short Rossby waves with eastward group velocity are not initially generated within this region. Instead, long Rossby waves with westward group velocity are generated to the east of the region of interest, either directly or as the result of reflections of Kelvin and Yanai waves from the eastern boundary. Eventually
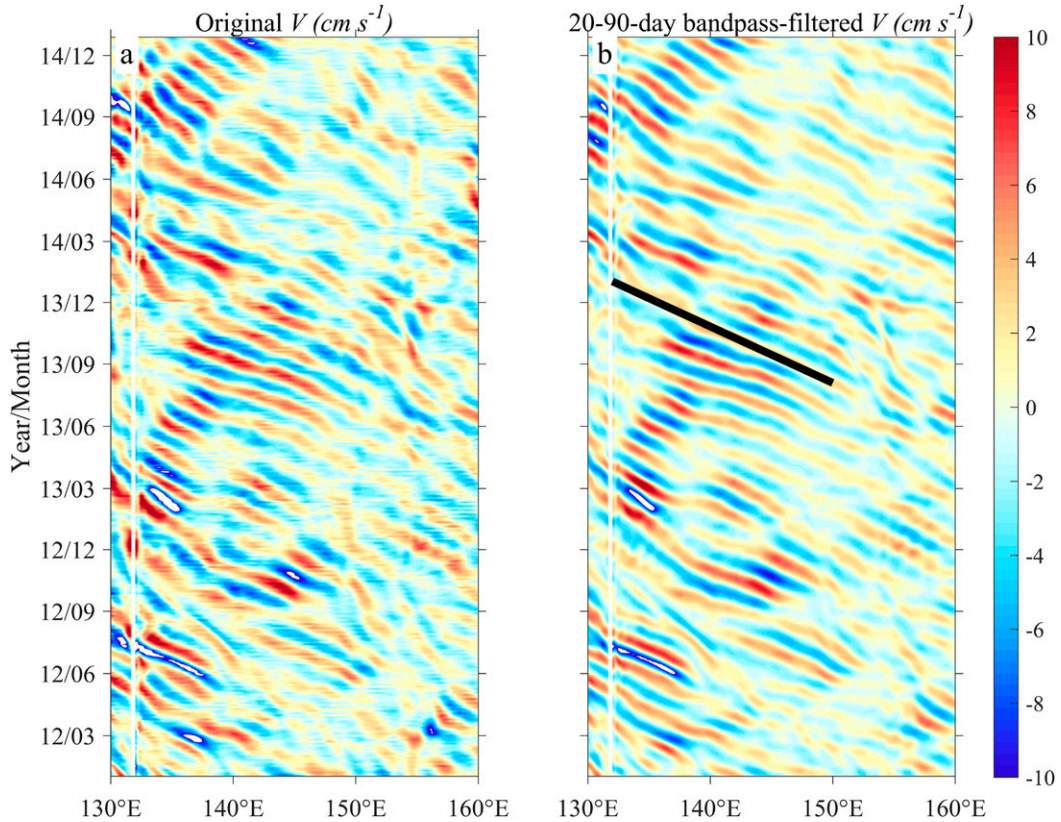
FIG. 5. Time–longitude variations of (a) original and (b) 20–90-day bandpass-filtered OFES V at 1200 m along 4.5°N during 2012–14. In (b), the black solid line denotes the phase propagation inferred from the wave crest line.

these long Rossby waves reach the western boundary and reflect there, creating the short Rossby waves observed to be dominant in the region of interest (Fig. 7e). We have also performed the simulation with a wind

stress that extends over the entire basin and found a similar response (figure not shown).

First, we examine the meridional distributions of V at the 50-day period for the odd mode case (Figs. 7d,e). In the open region to the east of the southern boundary,
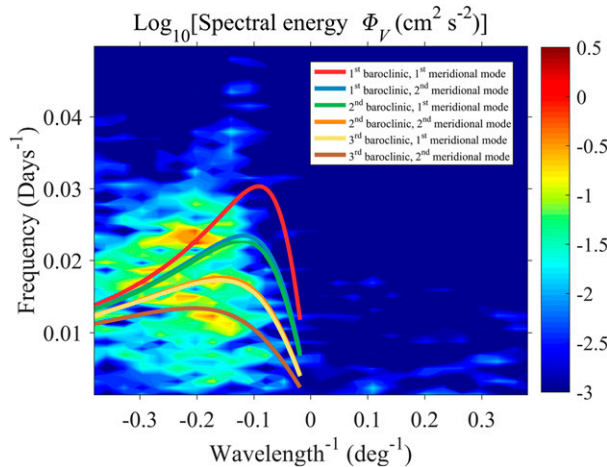

FIG. 6. Logarithm of wavelength–frequency spectral energy of OFES V along 4.5°N between 128° and 160°E. For reference, the theoretical dispersion relation curves of the equatorially trapped Rossby waves in the open ocean [Eq. (4)] are depicted.

TABLE 1. The list of characteristic speeds c_n (n indicates the nth baroclinic mode), wavelengths λ, and phase velocities C_p for the first four baroclinic modes corresponding to the background vertical density profile at 4.5°N, 142°E. The negative values indicate westward speed, and subscripts 1 and 2 for λ and C_p denote the first and second meridional modes, respectively.

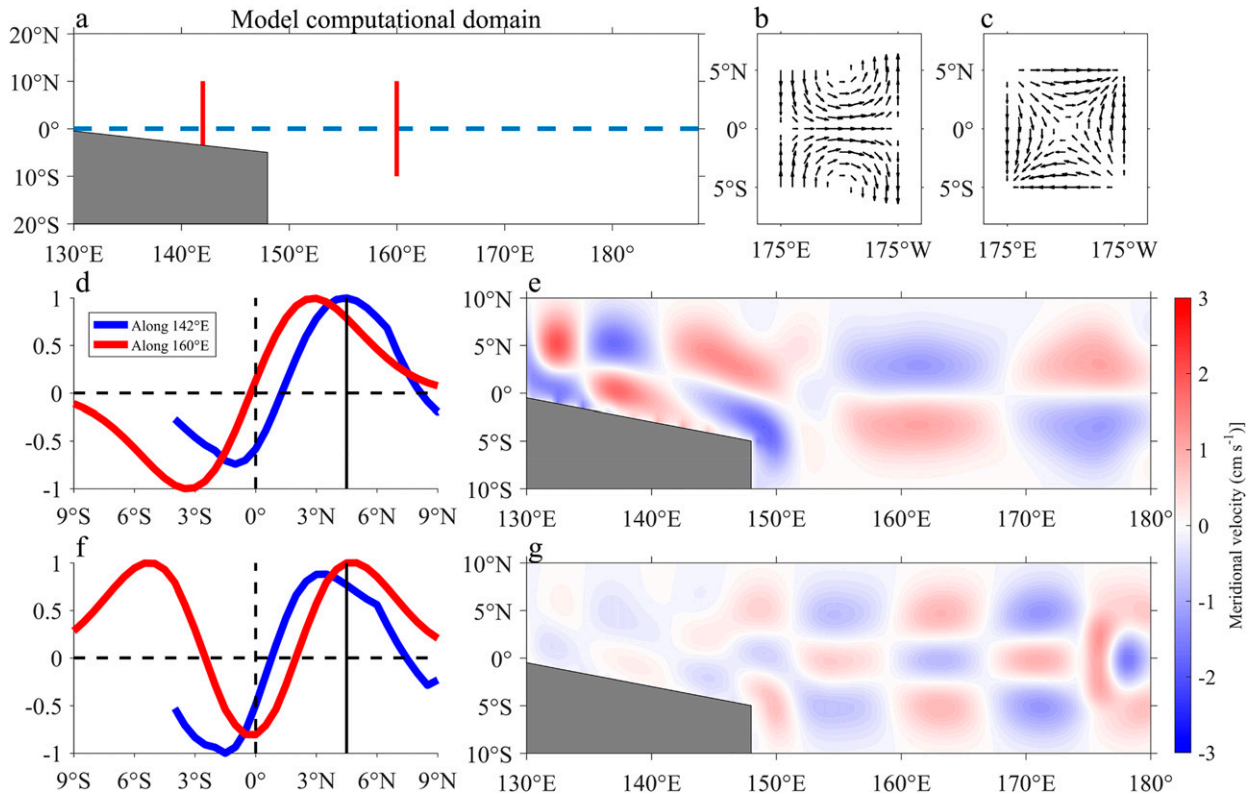| n	1	2	3	4
c_n (cm s^{-1})	255.8	143.7	83.0	67.1
		Period = 45 days		
λ_1 (km)	−530	−730	—	—
C_{p1} (cm s^{-1})	−13.64	−18.75	—	—
λ_2 (km)	−670	—	—	—
C_{p2} (cm s^{-1})	−17.22	—	—	—
		Period = 60 days		
λ_1 (km)	−360	−400	−530	—
C_{p1} (cm s^{-1})	−6.89	−7.75	−10.23	—
λ_2 (km)	−390	−500	—	—
C_{p2} (cm s^{-1})	−7.50	−9.62	—	—

FIG. 7. (a) The computational domain used in our 1.5-layer shallow water model. The gray shadow area indicates the solid boundary. Two kinds of wind stress fields introduced into the model to trigger the (b) odd and (c) even mode cases. (d),(f) The meridional structures of V in the odd and even mode cases along 142°E (blue lines) and 160°E (red lines), respectively. Black solid lines indicates 4.5°N. Snapshots of horizontal distribution of V associated with (e) odd and (g) even mode cases.

such as along 160°E, the meridional distributions of V are opposite between two hemispheres, and show peaks at 3°N and 3°S (Fig. 7d). This two-peak structure suggests the dominant role of the first meridional mode among all odd numbered meridional modes for this particular forcing. In the region north of the tilted boundary, the zonal wavelength contracts. Along 142°E, in the region with the southern boundary, the meridional distribution of V shifts northward, and shows peaks

at 4.5°N and near the southern boundary. This northward shift is also apparent in the spectral energy (Fig. 8a) for the odd mode case. Two ISV energy bands of V are apparent at 160°E, but these become displaced to the north as one moves to the west and into the region of the sloping boundary. The energy peaks also become intensified in this western part of the domain. At 142°E, the peaks are located near the equator and near 4.5°N, as in the observations and the OFES model.

TABLE 2. The detailed settings for wind stress fields in the 1.5-layer model. The terms τ_x and τ_y denote the zonal and meridional components of wind stresses, and x and y represent longitude and latitude of the grid point in the model, respectively.

	Odd mode case		Even mode case	
Area	$|y| < 5°$ and $|x - 180°| < 5°$	Other region	$|y| < 5°$ and $|x - 180°| < 5°$	Other region
τ_x	$\cos\left(\dfrac{t}{50\,\text{days}}2\pi\right) \times \cos\left(\dfrac{y}{10}\pi\right)$ $\times \cos\left(\dfrac{x-180}{10}\pi\right) \times 0.1\,\text{N m}^{-2}$	0	$\cos\left(\dfrac{t}{50\,\text{days}}2\pi\right) \times \sin\left(\dfrac{y}{10}\pi\right)$ $\times \cos\left(\dfrac{x-180}{10}\pi\right) \times 0.1\,\text{N m}^{-2}$	0
τ_y	$\cos\left(\dfrac{t}{50\,\text{days}}2\pi\right) \times \sin\left(\dfrac{y}{10}\pi\right)$ $\times \sin\left(\dfrac{x-180}{10}\pi\right) \times 0.1\,\text{N m}^{-2}$	0	$\cos\left(\dfrac{t}{50\,\text{days}}2\pi\right) \times \cos\left(\dfrac{y}{10}\pi\right)$ $\times \sin\left(\dfrac{x-180}{10}\pi\right) \times 0.1\,\text{N m}^{-2}$	0

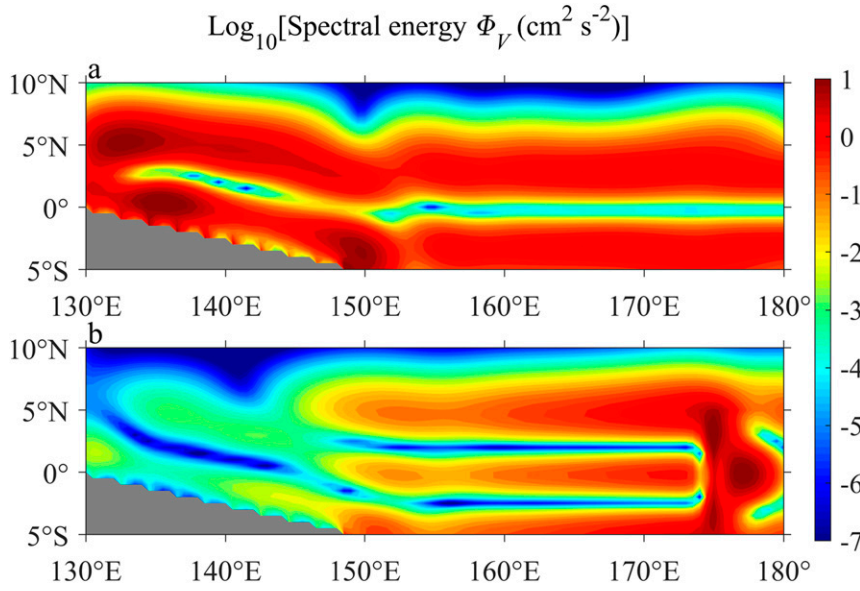$$\text{Log}_{10}[\text{Spectral energy } \Phi_V \text{ (cm}^2 \text{ s}^{-2})]$$

FIG. 8. The spectral energy distributions of 50-day oscillation for (a) odd and (b) even mode cases.

The situation for the even mode case is quite different, as shown in Figs. 7f and 7g. At 160°E, the meridional distribution of V is symmetric with respect to the equator, and shows three peaks at 5°S, the equator and 5°N (Fig. 7f). Three energy bands are also seen at above three latitudes (Fig. 8b), a pattern conforming to the meridional structure of the meridional mode two. To the west, at 142°E, the meridional structure shows only two peaks, the locations of which are shifted southward to 3°N and 1.5°S. Correspondingly, the three energy bands are reduced to two and become weakened from the central basin to the western boundary region. In summary, the first meridional mode is primarily responsible for the main meridional structures apparent in the observations and the OFES model.

c. The vertical structure of ISV energy

The 1.5-layer model results suggest the dominant role of the first meridional mode Rossby wave, but the model cannot reproduce more complicated vertical structures or the vertical propagation of ISV energy. Thus, we return to the OFES model and examine the horizontal distribution of the OFES ISV energy for the 50-day period at 1200 m (Fig. 9a). Two separate ISV energy bands of V emanate from the western boundary and extend southeastward, paralleling the coastlines of Irian Jaya and Papua New Guinea. The bands are similar to what is seen in the 1.5-layer model (Fig. 8a), though they are not continuous, due to the more realistic stratification, topography and presence of equatorial currents in OFES. The northern band crosses the mooring array

(142°E) between 4° and 6°N. This crossing conforms to that shown in Figs. 3a and 4a. The second band crosses the mooring array at approximate 1.5°S.

The depth–longitude variation of ISV energy for the 50-day period indicates vertical propagation (Fig. 9b), as suggested by a vertical section plotted along the northern band (black line in Fig. 9a). The ISV energy shows large values on both sides of Palau Island, particularly on the eastern side, but the energy band extends well east of the island and descends to greater depths. The energy intensity at 142°E increases from 250 to 800 m and then decreases for depths deeper than 800 m. The ray path of the short equatorial Rossby waves in the zonal–vertical $(x–z)$ plane can be calculated from

$$\frac{dx}{dz} = \frac{\partial\omega/\partial k}{\partial\omega/\partial m} = \frac{2k + \beta/\omega}{(2j+1)\beta}N, \tag{7}$$

where m is the vertical wavenumber (Kessler and McCreary 1993) and k is calculated from the zonal wavelength in the OFES model results. The distribution of large ISV energy in red and yellow patches generally follows the ray path of the first meridional mode short Rossby wave with a period of 50 days (black solid line in Fig. 9b). The combination of the 1.5-layer model and the OFES model results suggests that the meridional structure of first meridional mode short Rossby wave influenced by the presence of a tilted southern boundary is responsible for southeastward energy propagation, and thus generates a primary peak of intermediate ISV energy at 4.5°N along 142°E.
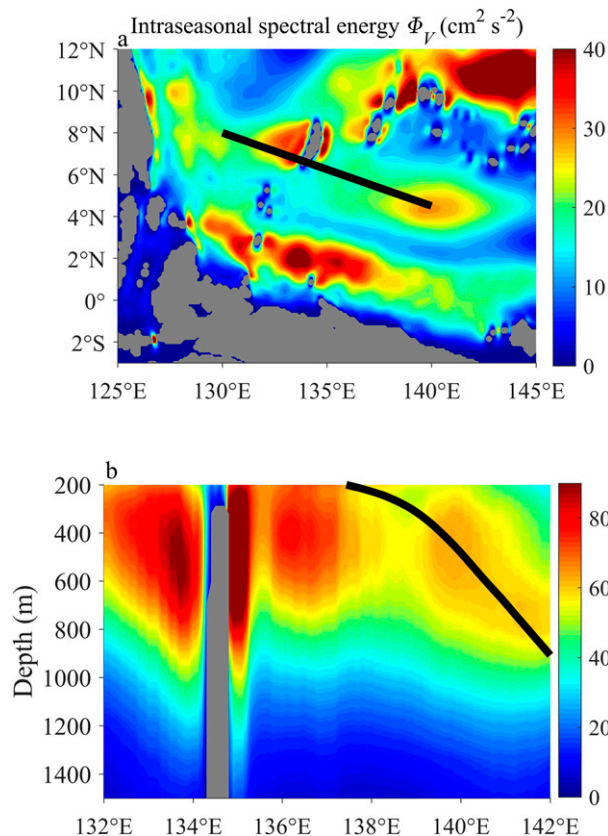
FIG. 9. (a) Horizontal distribution of the intraseasonal spectral energy for 50-day period at 1200-m depth based on OFES outputs. (b) The vertical section of the intraseasonal spectral energy along the black line in (a), representing the energy propagating path. In (b), the black solid line denotes the ray path of the first meridional mode short Rossby wave based on Eq. (7). The gray area indicates the geometry.
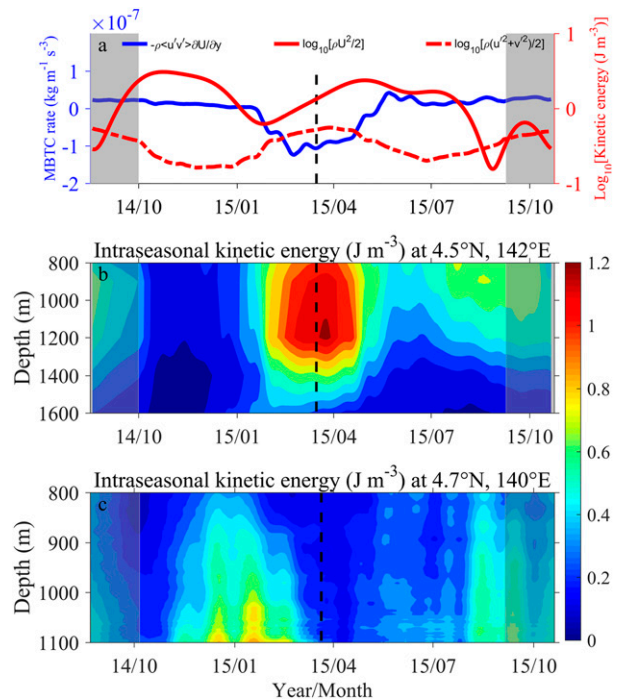

FIG. 10. (a) Meridional component of barotropic conversion (MBTC) rate associated with mean zonal flow (blue solid line), logarithm of mean kinetic energy of low-pass-filtered zonal flow (M-KE; red solid line) and logarithm of mean ISV kinetic energy (ISV-KE; red dashed line). The values come from observations at 1200-m depth, 142°E, and represent averages over 3°–6°N. The intraseasonal kinetic energy (b) over 800–1600 m at 4.5°N, 142°E and (c) over 800–1100 m at 4.7°N, 140°E. In (a)–(c), black dashed lines indicate the time of maximum energy burst at 4.5°N, 142°E for reference. Edge effects in the filtering contaminate the signal in the gray shaded areas.

5. Discussion of the linkage between intraseasonal variability and mean flow

Next, we discuss the connection between ISV energy and the mean flow in the intermediate layer. The observed average values of mean zonal flow kinetic energy (M-KE), ISV kinetic energy (ISV-KE), and the meridional component of barotropic conversion (MBTC) rate at 1200 m over the region of 3°–6°N along 142°E are depicted in Fig. 10a. The observed M-KE and ISV-KE at 3°, 4.5°, and 6°N are averaged to obtain regional means. The MBTC rate can be calculated via (Qiu et al. 2015; Wang et al. 2016a)

$$-\rho\langle u'v'\rangle\frac{\partial\overline{U}}{\partial y} - \rho\langle v'v'\rangle\frac{\partial\overline{V}}{\partial y}, \qquad (8)$$

where ρ is the ocean density, u' and v' are the 90-day high-pass-filtered zonal and meridional current anomalies, $\partial\overline{U}/\partial y$ and $\partial\overline{V}/\partial y$ are meridional shears of the 90-day low-pass-filtered zonal and meridional velocities ($\overline{U}$ and $\overline{V}$), and the angle brackets indicate the calculation of a 45-day running mean. Quantities of u', v', and ρ are obtained using mooring data at 4.5°N. For the calculations of $\partial\overline{U}/\partial y$ and $\partial\overline{V}/\partial y$, we first fit second-order polynomial functions to the observed $\overline{U}$ and $\overline{V}$ at 3°, 4.5°, and 6°N to obtain meridional profiles of velocities, and then compute meridional shears from the derivatives of the fitted polynomials. Negative MBTC indicates that the energy has been transferred from the ISV-KE to M-KE through barotropic instability, and vice versa. The lack of a mooring array in the zonal direction puts a constraint on calculating the horizontal derivative of velocities and density; thus, the zonal terms in barotropic and baroclinic conversions cannot be estimated. Additionally, the meridional component of baroclinic conversion rate ($10^{-9}\,\mathrm{kg\,m^{-1}\,s^{-3}}$) is at much lower level than MBTC ($10^{-7}\,\mathrm{kg\,m^{-1}\,s^{-3}}$), so the influence of the meridional component of baroclinic conversion is ignored in our analysis.

The relationships among M-KE, ISV-KE, and MBTC rate can be roughly established during the period of inverse energy cascade in Fig. 10a. The ISV-KE {red dashed line, $\log_{10}[\rho(u'^2 + v'^2)/2]$} remains at the low value of $0.2\,\mathrm{J\,m^{-3}}$ before January 2015, rises to the peak value of $0.56\,\mathrm{J\,m^{-3}}$ in mid-March, and then is reduced to the low value again. During the period from February to May, the MBTC term (solid blue line, $-\rho\langle u'v'\rangle \partial\overline{U}/\partial y$) becomes negative, indicating an energy transfer to the mean zonal flow. The contribution from the other component of MBTC ($-\rho\langle v'v'\rangle \partial\overline{V}/\partial y$) is negligible during the entire period (not shown). Thus, the ISV energy is being transferred to the background zonal flows through barotropic instability when the ISV energy itself is large. It is encouraging that the time variation of M-KE (red solid line, $\log_{10}\rho\overline{U}^2/2$) broadly supports the above mechanism. During the period from February to May 2015, a large ISV-KE and negative MBTC rate appears, and the M-KE correspondingly shows a persistent increasing trend; in further quantitative analysis, the MBTC energy is estimated at $-0.96\,\mathrm{J\,m^{-3}}$ by integrating over this period, generally consistent with the increase in M-KE of approximately $1.2\,\mathrm{J\,m^{-3}}$. This suggests that intermediate ISV energy coming from the remote upper ocean may contribute to the formation of the intermediate zonal jets. For the periods December 2014–February 2015, and July–September 2015, the MBTC rate is weakly positive, suggesting that M-KE should decrease. Although this is generally observed during these periods, the decrease rate of M-KE is greater than that can be accounted for by eddy-to-mean conversion rates that can be estimated using the available data. We leave this suggestive result to future investigators to clarify. It is hoped that our discussions here on new observations will stimulate oceanographers who are trying to solve the intermediate ocean circulation puzzle.

Figures 10b and 10c display observed ISV kinetic energy over 800–1600 m at 4.5°N, 142°E and over 800–1100 m at 4.7°N, 140°E. The strong ISV energy intensity occurs during January–February at 4.7°N, 140°E, two months earlier than the appearance of a strong ISV energy signal at 4.5°N, 142°E. This provides further evidence for the southeastward propagation of ISV energy by short Rossby waves, although locations of these two moorings do not strictly follow the black line in Fig. 9a.

6. Summary and conclusions

Based on a 1-yr mooring array observation of ocean currents along 142°E in the western tropical Pacific Ocean, the meridional structure of the intraseasonal variability (ISV) at intermediate depth is investigated. At 1200 m, the intermediate intraseasonal energy at periods around 45 days shows a primary peak at 4.5°N and a secondary peak near the equator. The vertical structure of ISV at 4.5°N, 142°E shows the presence of a maximum that lies between 900 and 1200 m and that is clearly separated from the near-surface stronger maximum. These characteristics are reproduced by the OFES global simulation and shown to exhibit very weak interannual variation. Time–longitude variation of OFES results further demonstrates that the intraseasonal energy at intermediate depths is associated with short Rossby waves with westward phase speed but southeastward and downward group velocity. Further analysis based on equatorial wave theory suggests that the first three baroclinic modes of Rossby waves account for the vertical propagation of ISV energy in the western Pacific Ocean.

A 1.5-layer model is employed to assess the roles of different meridional modes of Rossby waves in the observed meridional structure of ISV. Two kinds of wind stress fields are introduced into the model to trigger the odd and even numbered meridional modes of equatorial Rossby waves that would exist in an unbounded ocean. In the model results, we find out that the meridional structure of first meridional mode Rossby wave is altered by the presence of a tilted southern boundary and thus made consistent with the observed distribution of ISV in the western Pacific. The OFES outputs further support the above conclusions and detail the scenario of energy propagation in the zonal–vertical plane. The ISV energy is demonstrated to be carried from the remote near-surface to the intermediate depth of mooring location through the downward- and southeastward-propagating beam of short Rossby waves. This generation mechanism of the intermediate ISV is somewhat different from those mentioned previously (in the introduction section), which suggest that the intermediate ISV is generated at depth near the deep western boundary (Ascani et al. 2015) or the ridge topography (McPhaden and Gill 1987; Bunge et al. 2008), or is propagated from remote surface through Yanai (Ascani et al. 2010) or Kelvin waves (Matthews et al. 2007).

We also find evidence of the importance of the intermediate ISV on the formation of intermediate zonal jets. During the period of large ISV energy, a large negative MBTC rate appears, followed by an increase in mean zonal flow kinetic energy. It is suggested that the ISV energy can be transferred to the mean flow through barotropic instability. However, a full understanding of energy exchange between the middepth flow and ISV is still needed. It is hoped that our study is valuable in expanding the knowledge of intermediate and deep ocean dynamics, and stressing the importance of correctly simulating the intermediate ISV on the zonal jets. Such variability may have consequences for the zonal

distribution of biogeochemical properties (e.g., Dietze and Loeptien 2013; Getzlaff and Dietze 2013).

REFERENCES

Ascani, F., E. Firing, P. Dutrieux, J. P. McCreary, and A. Ishida, 2010: Deep equatorial ocean circulation induced by a forced–dissipated Yanai beam. *J. Phys. Oceanogr.*, **40**, 1118–1142, https://doi.org/10.1175/2010JPO4356.1.

——, ——, J. P. McCreary, P. Brandt, and R. J. Greatbatch, 2015: The deep equatorial ocean circulation in wind-forced numerical solutions. *J. Phys. Oceanogr.*, **45**, 1709–1734, https://doi.org/10.1175/JPO-D-14-0171.1.

Bonjean, F., and G. S. E. Lagerloef, 2002: Diagnostic model and analysis of the surface currents in the tropical Pacific Ocean. *J. Phys. Oceanogr.*, **32**, 2938–2954, https://doi.org/10.1175/1520-0485(2002)032<2938:DMAAOT>2.0.CO;2.

Bunge, L., C. Provost, B. L. Hua, and A. Kartavtseff, 2008: Variability at intermediate depths at the equator in the Atlantic Ocean in 2000–06: Annual cycle, equatorial deep jets, and intraseasonal meridional velocity fluctuations. *J. Phys. Oceanogr.*, **38**, 1794–1806, https://doi.org/10.1175/2008JPO3781.1.

Cravatte, S., W. S. Kessler, and F. Marin, 2012: Intermediate zonal jets in the tropical Pacific Ocean observed by Argo floats. *J. Phys. Oceanogr.*, **42**, 1475–1485, https://doi.org/10.1175/JPO-D-11-0206.1.

——, E. Kestenare, F. Marin, P. Dutrieux, and E. Firing, 2017: Subthermocline and intermediate zonal currents in the tropical Pacific Ocean: Paths and vertical structure. *J. Phys. Oceanogr.*, **47**, 2305–2324, https://doi.org/10.1175/JPO-D-17-0043.1.

Delcroix, T., G. Eldin, M. H. Radenac, J. Toole, and E. Firing, 1992: Variation of the western equatorial Pacific Ocean, 1986–1988. *J. Geophys. Res.*, **97**, 5423–5445, https://doi.org/10.1029/92JC00127.

Dietze, H., and U. Loeptien, 2013: Revisiting "nutrient trapping" in global coupled biogeochemical ocean circulation models. *Global Biogeochem. Cycles*, **27**, 265–284, https://doi.org/10.1002/gbc.20029.

d'Orgeville, M., B. L. Hua, and H. Sasaki, 2007: Equatorial deep jets triggered by a large vertical scale variability within the western boundary layer. *J. Mar. Res.*, **65**, 1–25, https://doi.org/10.1357/002224007780388720.

Duchon, C. E., 1979: Lanczos filtering in one and two dimensions. *J. Appl. Meteor.*, **18**, 1016–1022, https://doi.org/10.1175/1520-0450(1979)018<1016:LFIOAT>2.0.CO;2.

Farrar, J. T., 2008: Observations of the dispersion characteristics and meridional sea level structure of equatorial waves in the Pacific Ocean. *J. Phys. Oceanogr.*, **38**, 1669–1689, https://doi.org/10.1175/2007JPO3890.1.

——, 2011: Barotropic Rossby waves radiating from tropical instability waves in the Pacific Ocean. *J. Phys. Oceanogr.*, **41**, 1160–1181, https://doi.org/10.1175/2011JPO4547.1.

——, and R. A. Weller, 2006: Intraseasonal variability near 10°N in the eastern tropical Pacific Ocean. *J. Geophys. Res.*, **111**, C05015, https://doi.org/10.1029/2005JC002989.

Getzlaff, J., and H. Dietze, 2013: Effects of increased isopycnal diffusivity mimicking the unresolved equatorial intermediate current system in an Earth system climate model. *Geophys. Res. Lett.*, **40**, 2166–2170, https://doi.org/10.1002/grl.50419.

Gouriou, Y., T. Delcroix, and G. Eldin, 2006: Upper and intermediate circulation in the western equatorial Pacific Ocean in October 1999 and April 2000. *Geophys. Res. Lett.*, **33**, L10603, https://doi.org/10.1029/2006GL025941.

Hua, B. L., M. d'Orgeville, M. D. Fruman, C. Menesguen, R. Schopp, P. Klein, H. Sasaki, 2008: Destabilization of mixed Rossby gravity waves and the formation of equatorial zonal jets. *J. Fluid Mech.*, **610**, 311–341, https://doi.org/10.1017/S0022112008002656.

Johnson, G. C., B. M. Sloyan, W. S. Kessler, and K. E. McTaggart, 2002: Direct measurements of upper ocean currents and water properties across the tropical Pacific during the 1990s. *Prog. Oceanogr.*, **52**, 31–61, https://doi.org/10.1016/S0079-6611(02)00021-6.

Kessler, W. S., and B. A. Taft, 1987: Dynamic heights and zonal geostrophic transports in the central tropical Pacific during 1979–84. *J. Phys. Oceanogr.*, **17**, 97–122, https://doi.org/10.1175/1520-0485(1987)017<0097:DHAZGT>2.0.CO;2.

——, and J. P. McCreary, 1993: The annual wind-driven Rossby wave in the subthermocline equatorial Pacific. *J. Phys. Oceanogr.*, **23**, 1192–1207, https://doi.org/10.1175/1520-0485(1993)023<1192:TAWDRW>2.0.CO;2.

Kleeman, R., J. P. McCreary, and B. A. Klinger, 1999: A mechanism for generating ENSO decadal variability. *Geophys. Res. Lett.*, **26**, 1743–1746, https://doi.org/10.1029/1999GL900352.

Lighthill, M. I., 1969: Dynamic response of the Indian Ocean to onset of the southwest monsoon. *Philos. Trans. Roy. Soc. London*, **A265**, 45–92, https://doi.org/10.1098/RSTA.1969.0040.

Masumoto, Y., and Coauthors, 2004: A fifty-year eddy-resolving simulation of the world ocean: Preliminary outcomes of OFES (OGCM for the Earth Simulator). *J. Earth Simul.*, **1**, 35–56.

Matsuno, T., 1966: Quasi-geostrophic motions in the equatorial area. *J. Meteor. Soc. Japan*, **44**, 25–43, https://doi.org/10.2151/jmsj1965.44.1_25.

Matthews, A. J., P. Singhruck, and K. J. Heywood, 2007: Deep ocean impact of a Madden-Julian Oscillation observed by Argo floats. *Science*, **318**, 1765–1769, https://doi.org/10.1126/science.1147312.

McPhaden, M., and A. Gill, 1987: Topographic scattering of equatorial Kelvin waves. *J. Phys. Oceanogr.*, **17**, 82–96, https://doi.org/10.1175/1520-0485(1987)017<0082:TSOEKW>2.0.CO;2.

Ménesguen, C., A. Delpech, F. Marin, S. Cravatte, R. Schopp, and Y. Morel, 2019: Observations and mechanisms for the

formation of deep equatorial and tropical circulation. *Earth Space Sci.*, **6**, 370–386, https://doi.org/10.1029/2018EA000438.

Moore, D., and J. P. McCreary, 1990: Excitation of intermediate-frequency equatorial waves at a western ocean boundary: With application to observations from the Indian Ocean. *J. Geophys. Res.*, **95**, 5219–5231, https://doi.org/10.1029/JC095iC04p05219.

Pedlosky, J., 1987: *Geophysical Fluid Dynamics*. 2nd ed. Springer, 710 pp.

Philander, S., 1977: The effects of coastal geometry on equatorial waves (forced waves in the Gulf of Guinea). *J. Mar. Res.*, **35**, 509–523.

Ponte, R. M., and D. S. Gutzler, 1992: 40–60 day oscillations in the western tropical Pacific: Results from an eddy-resolving global ocean model. *Geophys. Res. Lett.*, **19**, 1475–1478, https://doi.org/10.1029/92GL01640.

Qiu, B., S. Chen, and H. Sasaki, 2013: Generation of the north equatorial undercurrent jets by triad baroclinic Rossby wave interactions. *J. Phys. Oceanogr.*, **43**, 2682–2698, https://doi.org/10.1175/JPO-D-13-099.1.

——, ——, D. L. Rudnick, and Y. Kashino, 2015: A new paradigm for the North Pacific subthermocline low-latitude western boundary current system. *J. Phys. Oceanogr.*, **45**, 2407–2423, https://doi.org/10.1175/JPO-D-15-0035.1.

Reverdin, G., C. Frankignoul, E. Kestenare, and M. J. McPhaden, 1994: Seasonal variability in the surface currents of the equatorial Pacific. *J. Geophys. Res.*, **99**, 20 323–20 344, https://doi.org/10.1029/94JC01477.

Sasaki, H., M. Nonaka, Y. Masumoto, Y. Sasai, H. Uehara, and H. Sakuma, 2008: An eddy-resolving hindcast simulation of the quasiglobal ocean from 1950 to 2003 on the Earth Simulator. *High Resolution Numerical Modelling of the Atmosphere and Ocean*, K. Hamilton and W. Ohfuchi, Eds., Springer, 157–185.

Shankar, D., J. McCreary, W. Han, and S. Shetye, 1996: Dynamics of the East India coastal current: 1. Analytic solutions forced by interior Ekman pumping and local alongshore winds. *J. Geophys. Res.*, **101**, 13 975–13 991, https://doi.org/10.1029/96JC00559.

Wang, F., Y. Li, and J. Wang, 2016a: Intraseasonal variability of the surface zonal currents in the western tropical Pacific Ocean: Characteristics and mechanisms. *J. Phys. Oceanogr.*, **46**, 3639–3660, https://doi.org/10.1175/JPO-D-16-0033.1.

——, J. Wang, C. Guan, Q. Ma, and D. Zhang, 2016b: Mooring observations of equatorial currents in the upper 1000 m of the western Pacific Ocean during 2014. *J. Geophys. Res. Oceans*, **121**, 3730–3740, https://doi.org/10.1002/2015JC011510.

Wyrtki, K., 1974: Sea level and the seasonal fluctuations of the equatorial currents in the western Pacific Ocean. *J. Phys. Oceanogr.*, **4**, 91–103, https://doi.org/10.1175/1520-0485(1974)004<0091:SLATSF>2.0.CO;2.

——, and R. Kendall, 1967: Transports of the Pacific equatorial countercurrent. *J. Geophys. Res.*, **72**, 2073–2076, https://doi.org/10.1029/JZ072i008p02073.

Yang, J., and J. F. Price, 2000: Water-mass formation and potential vorticity balance in an abyssal ocean circulation. *J. Mar. Res.*, **58**, 789–808, https://doi.org/10.1357/002224000321358918.

Zang, X., L. L. Fu, and C. Wunsch, 2002: Observed reflectivity of the western boundary of the equatorial Pacific Ocean. *J. Geophys. Res.*, **107**, 3150, https://doi.org/10.1029/2000JC000719.